

This work was written as part of one of the author's official duties as an Employee of the United States Government and is therefore a work of the United States Government. In accordance with 17 U.S.C. 105, no copyright protection is available for such works under U.S. Law. Access to this work was provided by the University of Maryland, Baltimore County (UMBC) ScholarWorks@UMBC digital repository on the Maryland Shared Open Access (MD-SOAR) platform.

Please provide feedback

Please support the ScholarWorks@UMBC repository by emailing scholarworks-group@umbc.edu and telling us what having access to this work means to you and why it's important to you. Thank you.



The RS CVn-type Star GT Mus Shows Most Energetic X-Ray Flares Throughout the 2010s

Ryo Sasaki^{1,2}, Yohko Tsuboi¹, Wataru Iwakiri^{1,2}, Satoshi Nakahira³, Yoshitomo Maeda³, Keith Gendreau⁴, Michael F. Corcoran^{5,6}, Kenji Hamaguchi^{5,7}, Zaven Arzoumanian⁴, Craig B. Markwardt⁴, Teruaki Enoto⁸, Tatsuki Sato¹, Hiroki Kawai¹, Tatehiro Mihara², Megumi Shidatsu⁹, Hitoshi Negoro¹⁰, and Motoko Serino¹¹

¹ Department of Physics, Chuo University, 1-13-27 Kasuga, Bunkyo-ku, Tokyo 112-8551, Japan; sasaki@phys.chuo-u.ac.jp, tsuboi@phys.chuo-u.ac.jp

² RIKEN, 2-1 Hirosawa, Wako, Saitama 351-0198, Japan

³ Institute of Space and Astronautical Science, Japan Aerospace Exploration Agency, 3-1-1 Yoshinodai, Chuo-ku, Sagami-hara, Kanagawa 252-5210, Japan

⁴ X-ray Astrophysics Laboratory, NASA/Goddard Space Flight Center, Greenbelt, MD 20771, USA

⁵ CREST & the X-ray Astrophysics Laboratory, NASA/Goddard Space Flight Center, Greenbelt, MD 20771, USA

⁶ Institute for Astrophysics and Computational Science, The Catholic University of America, 200 Hannan Hall, Washington, DC 20064, USA

⁷ Department of Physics, University of Maryland Baltimore County, 1000 Hilltop Circle, Baltimore, MD 21250, USA

⁸ Extreme Natural Phenomena RIKEN Hakubi Research Team, RIKEN Cluster for Pioneering Research, 2-1 Hirosawa, Wako, Saitama 351-0198, Japan

⁹ Department of Physics, Ehime University, 2-5, Bunkyocho, Matsuyama, Ehime 790-8577, Japan

¹⁰ Department of Physics, Nihon University, 1-8 Kanda-Surugadai, Chiyoda-ku, Tokyo 101-8308, Japan

¹¹ Department of Physics and Mathematics, Aoyama Gakuin University, 5-10-1 Fuchinobe, Chuo-ku, Sagami-hara, Kanagawa 252-5258, Japan

Received 2020 May 27; revised 2021 January 17; accepted 2021 January 18; published 2021 March 23

Abstract

We report that the RS CVn-type star GT Mus (HR 4492, HD 101379+HD 101380) was the most active star in the X-ray sky in the last decade in terms of the scale of recurrent energetic flares. We detected 11 flares from GT Mus in 8 yr of observations with the Monitor of All-sky X-ray Image (MAXI) from 2009 August to 2017 August. The detected flare peak luminosities were $1\text{--}4 \times 10^{33}$ erg s⁻¹ in the 2.0–20.0 keV band for its distance of 109.6 pc. Our timing analysis showed long durations ($\tau_r + \tau_d$) of 2–6 days with long decay times (τ_d) of 1–4 days. The released energies during the decay phases of the flares in the 0.1–100 keV band were in the range of $1\text{--}11 \times 10^{38}$ erg, which are at the upper end of the observed stellar flare. The released energies during the whole duration were in the range of $2\text{--}13 \times 10^{38}$ erg in the same band. We carried out X-ray follow-up observations for one of the 11 flares with the Neutron star Interior Composition Explorer (NICER) on 2017 July 18 and found that the flare cooled quasi-statically. On the basis of a quasi-static cooling model, the flare loop length is derived to be 4×10^{12} cm (or $60 R_\odot$). The electron density is derived to be 1×10^{10} cm⁻³, which is consistent with the typical value of solar and stellar flares ($10^{10\text{--}13}$ cm⁻³). The ratio of the cooling timescales between radiative (τ_{rad}) and conductive (τ_{cond}) cooling is estimated to be $\tau_{\text{rad}} \sim 0.1 \tau_{\text{cond}}$ from the temperature; thus, radiative cooling was dominant in this flare.

Unified Astronomy Thesaurus concepts: [Stellar x-ray flares \(1637\)](#); [Stellar activity \(1580\)](#); [Time series analysis \(1916\)](#)

Supporting material: data behind figure

1. Introduction

Stellar flares are thought to be a result of magnetic reconnection on a stellar surface (e.g., Shibata & Yokoyama 1999). The process has been actively studied in the case of solar flares, since we can see the flares directly. For the Sun, we can follow the evolution of X-ray emission from plasma loops, which trace the shape of magnetic fields, and once an abrupt ignition occurs, we see how plasma starts to fill the loops. As for the flares on stars other than the Sun, on the other hand, the same process has been inferred from the time variation of physical parameters.

Since the beginning of X-ray astronomy, stellar flares have been observed with many instruments (e.g., Einstein, ROSAT, GINGA, ASCA, etc.). These observations have detected the fast rise and slow decay in the light curves of stellar flares and that flare temperature peaks before the emission measure (EM), i.e., harder emission peaks before softer emission (e.g., Tsuboi et al. 1998), all of which are seen in the solar flares as well.

Through these studies, both RS CVn systems and young stellar objects have been recognized as active flare sources. As for the flares from RS CVn stars, in the last two decades, those from UZ Lib, HR 1099, σ Gem, λ And, and EI Eri were detected with XMM-Newton (Pandey & Singh 2012a); those

from HR 1099, II Peg, TZ CrB, XY UMa, and AR Lac were detected with Chandra (Nordon & Behar 2007; Drake et al. 2014; Gong et al. 2016); and those from II Peg were detected with Swift (Osten et al. 2007), for example. However, most of the studies were done with pointed observations, where the large flares can be detected only by chance, though there are some rare cases where the pointed observations started with a trigger by wide-field monitorings (e.g., a flare from II Peg observed with Swift; Osten et al. 2007).

Detections of large flares have increased thanks to the Monitor of All-sky X-ray Image (MAXI; e.g., Tsuboi et al. 2016). MAXI is an all-sky X-ray monitor that has been operating on the Japanese Experiment Module (JEM; Kibo) on the International Space Station (ISS) since 2009 August 15 (Matsuoka et al. 2009). It observes a large area of the sky once per 92 minute orbital cycle and makes it possible to search for transients effectively.

Tsuboi et al. (2016) analyzed stellar flares detected in two years of MAXI observations. The observed parameters of all of these MAXI/GSC flares are found to be near the upper range for observed stellar flares (see their Figures 4 and 5), with luminosities of $10^{31\text{--}34}$ ergs s⁻¹ in the 2–20 keV band, EMs of $10^{54\text{--}57}$ cm⁻³, e-folding times of 1 hr to 1.5 days, and total

radiative energies of 10^{34-39} erg. They found a universal correlation between the flare duration and peak X-ray luminosity, combining the X-ray flare data of nearby stars and the Sun (their Figure 5).

Among the MAXI-detected stellar flare sources, the RS CVn-type star GT Mus showed remarkably energetic flares with energies up to $\sim 10^{38}$ erg, repeatedly. So far, MAXI has detected flare candidates with the MAXI “nova-alert system” (Negoro et al. 2016), designed to detect transients from MAXI all-sky images in real time. The MAXI team reported nine flare candidates to the MAXI mailing list. Among them, they reported three candidates to *The Astronomer’s Telegram*¹² (Nakajima et al. 2010; Kanetou et al. 2015; Sasaki et al. 2016). One of them has already been reported in Tsuboi et al. (2016).

The quadruple system GT Mus (HR 4492) consists of two binary systems named HD 101379 and HD 101380, located at (R.A., Dec.)(J2000) = (11^h39^m29^s.497, $-65^{\circ}23'52''.0135$) at a distance of 109.594 pc (Gaia Collaboration et al. 2016, 2018). The two binaries (HD 101379 and HD 101380) are separated by 0 $''$.23, which is spatially resolved by speckle methods (McAlister et al. 1990).

The RS CVn-type single-lined spectroscopic binary HD 101379 (Strassmeier et al. 1988; McAlister et al. 1990) has a G5/8 giant primary with a radius of $16.56 R_{\odot}$ (Gaia Collaboration et al. 2016, 2018). This binary shows strong Ca II H, Ca II K, and variable H α emissions (Houk & Cowley 1975). Moreover, it shows a periodic photometric variation of 61.4 days, which dominates any other variations of GT Mus. This 61.4 day variation may be attributed to a rotational modulation of one or more starspots on HD 101379 (Murdoch et al. 1995). These features indicate high magnetic activity, which implies that the flare observed by MAXI may have originated on HD 101379.

The other system, HD 101380, is a binary consisting of an A0 and an A2 main-sequence star (Houk & Cowley 1975; Collier 1982). In the folded V-band GT Mus light curve, a small dip is detected (Murdoch et al. 1995). It is interpreted to be due to an eclipse of this binary with a period of 2.75 days. No variations by spots have ever been observed. Thus, it is feasible to speculate that HD 101379 has higher chromospheric activity than HD 101380.

All of the reported MAXI flares from GT Mus so far have been detected by the MAXI “nova-alert system” (Negoro et al. 2016). However, there is a real potential that some flares have been missed by this automated system. Given the current small number (23) in the MAXI stellar flare sample (Tsuboi et al. 2016) and the highly active nature of GT Mus, GT Mus provides a good opportunity to study the physical characteristics of stellar flares and their mechanism.

In this work, we carry out a detailed analysis of the MAXI data (Section 2) of GT Mus to search for X-ray flares. We successfully detect 11 flares (including the three that have already been reported), all of which show a total released energy of 10^{38} erg or higher, and perform a unified analysis for all of them (Section 3). In addition, we also carry out follow-up X-ray observations with the Neutron star Interior Composition Explorer (NICER, see Section 2; Gendreau et al. 2016) for one of the flares, perform time-resolved spectroscopy, and give much tighter constraints on the physical characteristics (Section 3). We then discuss the cooling process of the flare observed with NICER and also GT Mus flares in general in a

broader context (Section 4) before summarizing our results (Section 5).

2. Observations

2.1. MAXI

MAXI (Matsuoka et al. 2009) is an astronomical X-ray observatory mounted on the ISS. In this analysis, we used data from the Gas Slit Camera (Mihara et al. 2011) only, which is sensitive in the 2–30 keV band. It consists of 12 proportional counters, each of which employs carbon-wire anodes to provide one-dimensional position sensitivity. A pair of counters forms a single camera unit; hence, the instrument consists of six camera units. The six camera units are assembled into two groups whose fields of view (FoVs) are pointed toward the tangential direction of ISS’s motion along the Earth’s horizon and the zenith direction. The FoVs are $160^{\circ} \times 3^{\circ}$, which corresponds to 2% of the whole sky. These counters are not operated in the regions with high particle background, such as the South Atlantic Anomaly and at absolute latitudes higher than $\sim 40^{\circ}$, and in the vicinity of the Sun (within $\sim 5^{\circ}$). Hence, the Gas Slit Camera has an operating duty ratio of $\sim 40\%$ and scans about 85% of the whole sky per orbit of the ISS.

In this work, we used the MAXI on-demand system¹³ (Nakahira et al. 2013) to obtain images, light curves, and spectra. We extracted source photons from a circular region with a radius of $1^{\circ}.5$ centered on GT Mus, the area of which corresponds to the point-spread function of the Gas Slit Camera. The background photons were extracted from a circular region with a radius of $4^{\circ}.0$ centered at (R.A., Dec.)(J2000) = (11^h24^m3^s.7699, $-67^{\circ}4'42''.939$), excluding the source area of radius $2^{\circ}.0$ centered at the same position as the source region. Here the center of the background region was shifted slightly from that of the source region in order to avoid light leakage from nearby bright sources (Cen X-3 and V830 Cen).

2.2. NICER

We carried out follow-up observations of a GT Mus flare (FN 11) with NICER. NICER is a nonimaging X-ray detector installed on the ISS in 2017 June. The X-ray detector of NICER, the X-ray Timing Instrument (XTI; Prigozhin et al. 2012), consists of 56 coaligned X-ray concentrator optics (XRCs) and silicon-drift detectors (SDDs). Each XRC collects X-ray photons over a large geometric area from a 15 arcmin² area of sky. The XRCs concentrate photons onto the SDDs. The SDDs have a sensitivity in the 0.2–12 keV band with an energy resolution of 85 eV at 1 keV. The XTIs provide a large effective area of ~ 1900 cm² at 1.5 keV. In practice, out of 56 XRCs, 52 are operated in orbit.

The NICER follow-up observation was carried out for FN 11. The nova-alert system (Negoro et al. 2016) triggered a transient event from GT Mus on 2017 July 17 03:55 UT. The NICER follow-up observation started on 2017 July 18 17:00 UT, ~ 1.5 days after the trigger, and ended on 2017 July 21 14:36 UT. During the observation, the count rate decayed from 300 to 140 counts s⁻¹ in the 0.5–10.0 keV band. After 123 days from the MAXI trigger for FN 11, NICER observed GT Mus again (from 2017 November 18 to 2017 November 20). During the 3 day observation, the count rate was constant at ~ 43

¹² <http://astronomerstelegram.org/>

¹³ <http://maxi.riken.jp/mxondem/>

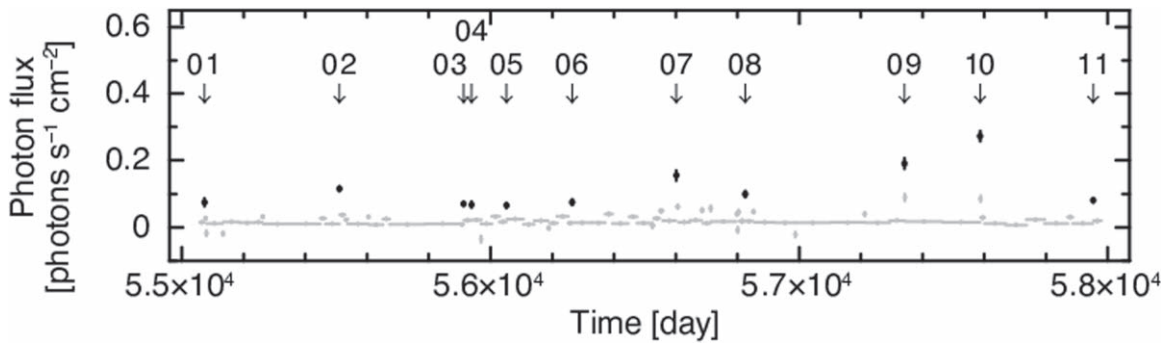


Figure 1. MAXI Bayesian block light curve for GT Mus spanning 8 yr (from 2009 August 15 to 2017 August 14). The downward-pointing arrows and black points show the epochs of the detected flares. The numbers above the arrows are the flare IDs, which correspond to the flare IDs in Table 1.

counts s^{-1} in the 0.5–10.0 keV band. No significant variability during the observation was detected (see Section 3.3 for details). Moreover, this is in agreement with the count rate of GT Mus in the XMM-Newton slew survey catalog (Freund et al. 2018), where *Web PIMMS*¹⁴ was employed for the count rate conversion. Because of that, we considered these data as the quiescent state of GT Mus.

With NICER, the spectral and temporal parameters of stellar flares can be determined with a much higher precision than with MAXI. NICER can swiftly respond to emergent observations because the ISS is in real-time contact for $\sim 70\%$ of a day, thanks to the Tracking and Data Relay Satellite.

In this work, we used all available GT Mus NICER data (observation IDs of 1100140101–1100140108). The data were calibrated and screened using HEASARC’s HEASOFT package (v6.25), which includes NICERDAS version 5, with NICER CALDB version 20181105. We processed the data using the task `nicerl2`, which generates a list of calibrated, accepted photons excluding periods of especially high background. By this cleaning, the data of observation ID 1100140105 were totally excluded. We extracted source spectra from the cleaned calibrated events.

We estimated background spectra for each of the extracted source spectra. The NICER background is produced by charged particles in the orbit of the ISS, which depends on magnetic cutoff rigidity and space weather conditions. In addition, optical loading from the sunlight falling on the detectors also contributes to background contamination. Most of them appear in the energy range below 0.4 keV. To estimate the background, we extracted NICER photon events from more than 970 ks of NICER blank-sky field observations that have similar cutoff rigidity, space weather, and Sun-angle conditions to those during the GT Mus observations. We accumulated spectra for these extracted background events and subtracted these spectra from the GT Mus spectra for spectral analysis. The estimated background rates were < 3 NICER XTI counts per second for all of the GT Mus observations. We conservatively used the 0.5–10 keV energy band in the analysis excluding the lowest and highest energy bands of the SDDs, in order to minimize the effects of the low-energy noise and large calibration uncertainty in the high-energy band above 10 keV.

3. Results

3.1. Flare Search with MAXI

We searched for flares from the MAXI GT Mus light curve using data from 2009 August 15 to 2017 August 14. First, we

applied an adaptive binning with a Bayesian block algorithm (Scargle et al. 2013) to a one-orbit light curve. Then, we identified statistically significant variations in the binned light curve with a simple nonparametric model (Figure 1), where the false-positive rate (i.e., probability of falsely detecting a change point) was set to $p_0 = 0.1$, which follows that the significance of a change point is 90% ($= 1 - p_0$). In Figure 1, the data points with time bins less than 0.15 day are deleted, because with such short time bins, the error of the background-subtracted events cannot be approximated to Gaussian. As flare candidates, the bins with a photon flux higher than $0.05 \text{ photons s}^{-1} \text{ cm}^{-2}$ are selected. We further filtered out dubious flare candidates using the spatial significance-checking method employed in Uzawa et al. (2011) and Tsuboi et al. (2016), in which the threshold significance was set to 5σ , where σ is the standard deviation of the X-ray counts of the background region in each MAXI image in the 2.0–10.0 keV band, scaled to the source area. We applied this method because the background count rates in the source region are higher than the source count rates in the quiescent state by a factor of 6. Consequently, we found 11 flares. Figure 1 shows the binned light curve with the 11 flares indicated, and Table 1 summarizes the parameters of the flares, including the 2.0–10.0 keV photon flux (see Section 3.2 for details) and the detection significance.

3.2. MAXI Light Curves and Spectra

For each of the 11 flares detected with MAXI, we performed time series and then spectral analyses. The duration, or e-folding time (τ_d), of each flare was determined from the 2.0–10.0 keV light curve with each time bin of half a day (Figure 2 and Table 2). Each light curve was fitted with a burst model, which consists of a linear rise followed by an exponential decay component with an additional constant component. The constant component was fixed to the photon flux of the quiescent emission, $0.013 \text{ photons s}^{-1} \text{ cm}^{-2}$, which was the average value of the over 100 day bin with the Bayesian block process.

The fitting model was expressed by

$$c(t) = 0.013 \quad (\text{for } t \leq \text{ST})$$

$$c(t) = \text{PC} \times \left(\frac{t - \text{ST}}{\text{PT} - \text{ST}} \right) \quad (\text{for } \text{ST} \leq t \leq \text{PT})$$

$$c(t) = \text{PC} \times \exp\left(-\frac{t - \text{PT}}{\tau_d} \right) \quad (\text{for } \text{PT} \leq t).$$

Here t , $c(t)$, ST, PT, and PC are time, count rates, the time when the count rate starts to increase, the time when the count rate is

¹⁴ <https://heasarc.gsfc.nasa.gov/cgi-bin/Tools/w3pimms/w3pimms.pl>

Table 1
Flare Epoch, Photon Flux, and Significance of Detection with MAXI

Flare ID	MJD ^a	UT ^b	Photon flux ^c (photons s ⁻¹ cm ⁻²)	Significance (σ)	Detection ^d Method
FN 01	55,073.691 ± 0.395	2009 Aug 30 16:35	0.08 ± 0.01	10.2	B
FN 02 ^e	55,510.517 ± 1.016	2010 Nov 10 08:34	0.12 ± 0.01	21.8	n, B
FN 03	55,912.883 ± 0.834	2011 Dec 17 21:11	0.07 ± 0.01	19.9	n, B
FN 04	55,938.629 ± 0.609	2012 Jan 12 15:05	0.07 ± 0.01	6.0	n, B
FN 05	56,051.871 ± 1.349	2012 May 4 20:54	0.07 ± 0.01	8.1	n, B
FN 06	56,264.539 ± 1.256	2012 Dec 3 12:56	0.08 ± 0.01	15.0	n, B
FN 07	56,602.168 ± 1.096	2013 Nov 6 04:01	0.15 ± 0.01	9.1	n, B
FN 08	56,824.965 ± 1.127	2014 Jun 16 23:09	0.10 ± 0.01	9.4	n, B
FN 09 ^f	57,341.297 ± 0.482	2015 Nov 15 07:07	0.19 ± 0.02	18.4	n, B
FN 10 ^g	57,585.996 ± 0.450	2016 Jul 16 23:54	0.27 ± 0.01	25.3	n, B
FN 11	57,952.516 ± 1.415	2017 Jul 18 12:22	0.08 ± 0.01	19.1	n, B

Notes.

^a Detection time of the flare in the adaptive binning (see the text for details).

^b Center time of the observation.

^c The energy band is in the 2.0–10.0 keV band.

^d Here “n” and “B” are the nova-alert system and the Bayesian block, respectively.

^e Nakajima et al. (2010) and Tsuboi et al. (2016).

^f Kanetou et al. (2015).

^g Sasaki et al. (2016).

the highest, and the count rate at PT, respectively. Because of the poor statistics, we were not able to determine ST and PT independently. Therefore, we fixed the peak time to the timing of the bin that has the highest photon flux. The exceptions are FN 01 and FN 05, whose rising phases were not observed. They were fitted instead with an exponential plus the constant function that describes the quiescent emission. The result showed that τ_d was 100–360 ks (1–4 days).

To determine the physical parameters of the individual flares, we analyzed the spectra at their peaks (see Figure 2 for the extracting time regions). In this analysis, we used the optically thin thermal plasma model *apec* (Smith et al. 2001) to fit the spectra. Given insufficient photon count statistics of the MAXI data, the metal abundance (Z) and interstellar absorption (N_{H}) in the model were fixed at $0.35 Z_{\odot}$ and $4.4 \times 10^{20} \text{ cm}^{-3}$, respectively, the values derived from the NICER time-resolved spectra (see Section 3.3 for details). The redshift was fixed at zero. The best-fit parameters are shown in Table 2. As a result of the fitting, the absorption-corrected flare peak luminosity in the 2–20 keV band ($L_{\text{X,peak}}$), temperature (kT), and EM were derived to be $1\text{--}4 \times 10^{33} \text{ erg s}^{-1}$, 4–11 keV, and $7\text{--}23 \times 10^{55} \text{ cm}^{-3}$, respectively. The released flare energies are separately shown, separated for the rise and decay phases. The flare energy during the rise phase (E_{rise}) was $3\text{--}16 \times 10^{37} \text{ erg}$, while that during the decay phase (E_{decay}) was $9\text{--}73 \times 10^{37} \text{ erg}$. Then, the emission in the decay phase is a majority of the energy released during the flare.

3.3. Analysis of the NICER Data

3.3.1. Flare Phase Analysis

NICER follow-up observations were performed for FN 11. The MAXI and NICER light curves in the 2.0–10.0 keV band of this flare are shown in Figure 3. Note that since the flare peak was missed with NICER, the MAXI peak data were added into Figure 3 after conversion to the NICER count rate with *Web PIMMS*.¹⁵ The NICER light curve was fitted with an

exponential function with the decay constant τ_d and a constant function, the latter of which was fixed to the NICER count rate in the quiescent state of $6.3 \text{ counts s}^{-1}$ in the 2.0–10.0 keV band. The period for the quiescent state is 3 days, from 2017 November 18 to 2017 November 20 (see Section 2.2). As a result, the decay constant τ_d was derived to be $174 \pm 3 \text{ ks}$. The reduced χ^2 (χ_{red}^2) and degrees of freedom (d.o.f.) were 1.8 and 10, respectively. The derived τ_d is consistent with the value derived from the MAXI light curve.

We performed time-resolved spectroscopy using the NICER data divided into 12 time intervals, which correspond to 12 ISS orbits, in the 0.5–10 keV band listed in Table 3. Figure 4 shows all of the time-resolved spectra and the best-fit model. Since the spectra are the sum of the quiescent and flare emissions, the modeling of the quiescent emission was fixed to the best-fit values given in Section 3.3.2. For the flare component, we first adopted an absorbed one-temperature optically thin thermal plasma model. Here we used *TBabs* (Wilms et al. 2000) and *apec* for the absorption and thin thermal plasma models, respectively. We also fixed the redshift to zero. However, this model was rejected with $\chi_{\text{red}}^2 > 2$. Then, we fitted the flare component with an absorbed two-temperature optically thin thermal plasma model with the metal abundances (Z) of the cool and hot plasma components assumed to be the same. The spectra were found to be well reproduced by this model. Table 3 and Figure 5 summarize the best-fit parameters and their time variations, respectively.

To check the potential time variations of these NICER spectral parameters, we fitted the time series of the hydrogen column density (N_{H}), Z , the kT of the cool component (kT_{cool}), and the EM of the cool component (EM_{cool}) with a constant model and found that all of these parameters were constant from flare to flare within the statistics. Table 4 shows the fitting results of the time series of the four parameters summarized in Table 3. By contrast, the parameters EM and kT of the hot component (EM_{hot} and kT_{hot}) showed clear declining trends. We study them in detail in Section 4.3.

¹⁵ <https://heasarc.gsfc.nasa.gov/cgi-bin/Tools/w3pimms/w3pimms.pl>

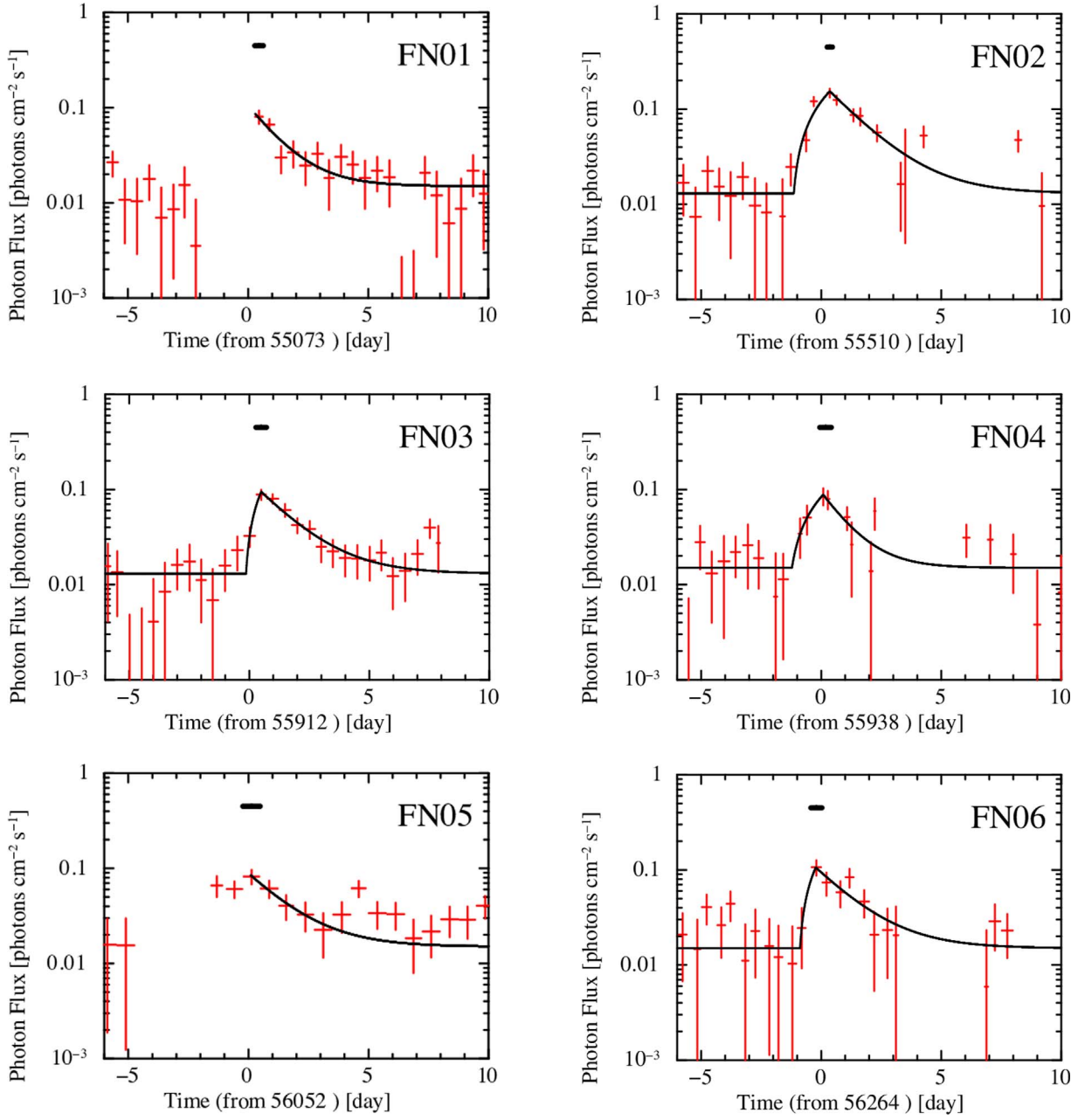


Figure 2. Light curves of the 11 flares of GT Mus detected with MAXI in the 2.0–10.0 keV band. The horizontal bar above the peak in each panel indicates the time interval from which the data are extracted to make the spectrum.

(The data used to create this figure are available.)

3.3.2. Quiescent State Analysis

We analyzed a quiescent-state spectrum as follows, using the time-averaged spectra for 3 days (from 2017 November 18 to 2017 November 20). The total exposure was 5 ks. The spectrum is shown in Figure 6. The spectrum could be fitted with the absorbed two thin thermal plasma models. As a result, the $kT_{\text{hot,q}}$, $\text{EM}_{\text{hot,q}}$, $kT_{\text{cool,q}}$, and $\text{EM}_{\text{cool,q}}$ values, where the subscript “q” means the quiescent state, were determined to be $3.13^{+0.06}_{-0.07}$ keV, $8.7^{+0.02}_{-0.01} \times 10^{54} \text{ cm}^{-3}$, 1.02 ± 0.01 keV, and $1.98 \pm 0.02 \times 10^{54} \text{ cm}^{-3}$, respectively. The parameters $N_{\text{H,q}}$ and Z_{q} were $5.9 \pm 0.3 \times 10^{20} \text{ cm}^2$ and $0.24^{+0.01}_{-0.02} Z_{\odot}$, respectively. The absorption-corrected quiescent X-ray luminosity in the 0.5–10.0 keV band was

$1.09 \pm 0.01 \times 10^{32} \text{ erg s}^{-1}$. The resultant χ^2_{red} and d.o.f. were 1.30 and 308, respectively. The cool component in the quiescent state can be intrinsically interpreted as the same as the cool component during the flare, having a similar temperature and EM (see Table 4).

4. Discussion

4.1. Flare Parameters of GT Mus

Using MAXI, we have detected 11 flares from GT Mus. From the X-ray spectroscopy, GT Mus was found to have large EMs and high plasma temperatures when it is flaring. Both of the parameters are confirmed to be located at the upper end of

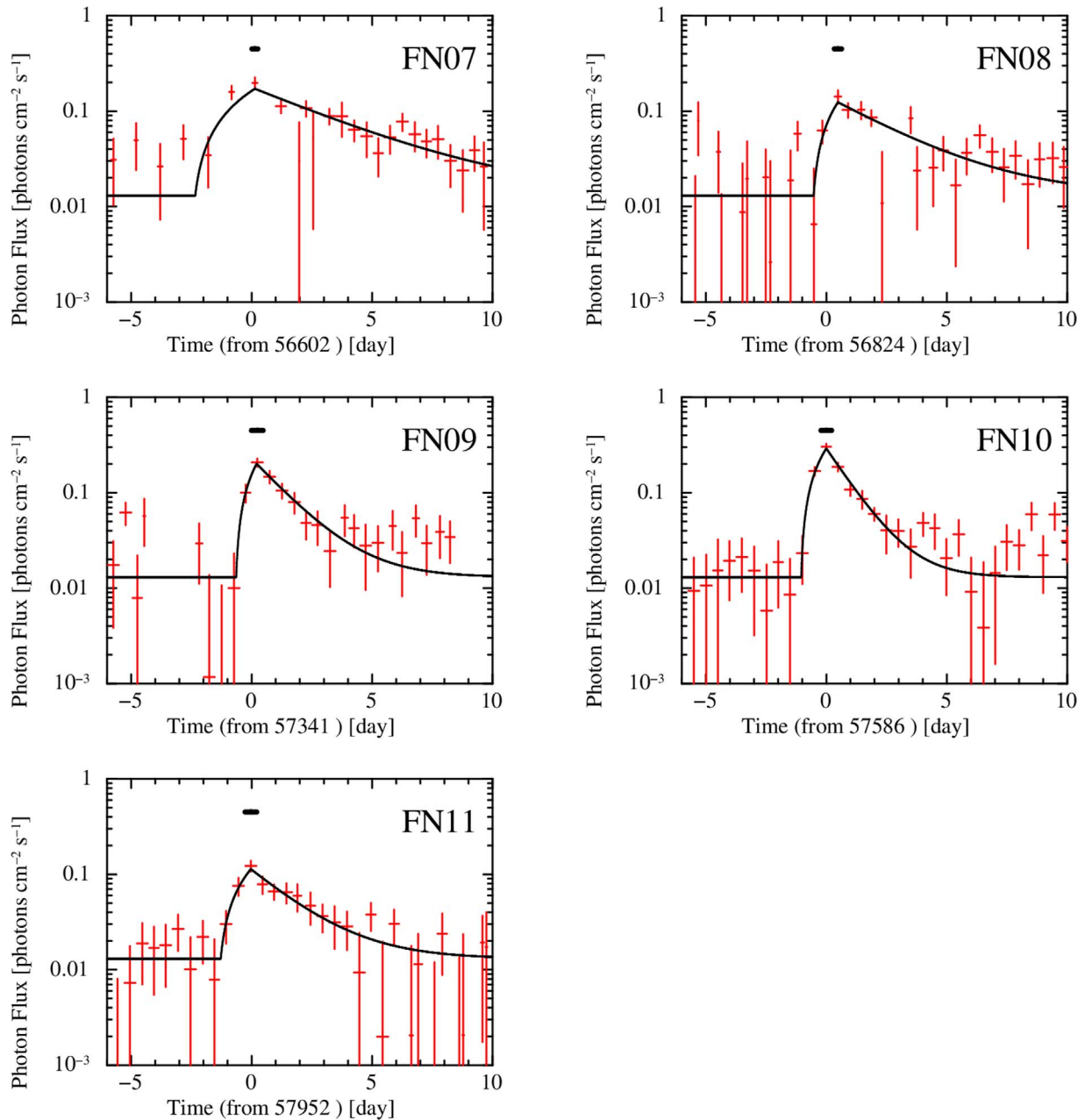


Figure 2. (Continued.)

the universal EM– kT correlation when we plot them into Figure 4 of Tsuboi et al. (2016).

The large EMs and the plasma temperatures give the large X-ray luminosities. The intrinsic X-ray luminosities in the 0.1–100 keV band, derived with the procedure described in the appendix of Tsuboi et al. (2016), are in the range of $2\text{--}5 \times 10^{33}$ erg s $^{-1}$. Our timing analysis showed long durations ($\tau_r + \tau_d$) of 2–6 days with long decay times (τ_d) of 1–4 days. We plotted both parameters on the τ_d – L_X diagram of Tsuboi et al. (2016; their Figure 5), adding the samples of RS CVn binaries detected with XMM-Newton (Pandey & Singh 2012a), Chandra (Nordon & Behar 2007; Drake et al. 2014; Gong et al. 2016), and Swift (Osten et al. 2007) after converting their luminosity ranges to the 0.1–100 keV band by using their

temperatures and EMs. The results are shown in Figure 8. In the diagram, the GT Mus flares are located at the upper end of the universal correlation obtained by Tsuboi et al. (2016).

The large X-ray bolometric luminosities and the decay timescales give the large X-ray released energies during the flares. In Figure 8, the dashed lines indicate the same energies. The energy released in the GT Mus flare decay phase is in the range of $1\text{--}11 \times 10^{38}$ erg in the 0.1–100 keV band, and that for the whole duration ($\tau_r + \tau_d$) is in the range of $2\text{--}13 \times 10^{38}$ erg. They are about more than an order of magnitude larger than the other observed stellar flares. We further show the observed flare energy distribution obtained with MAXI (this work and Tsuboi et al. 2016) in Figure 7. Here also, the extremely large energies of the GT Mus flares are shown.

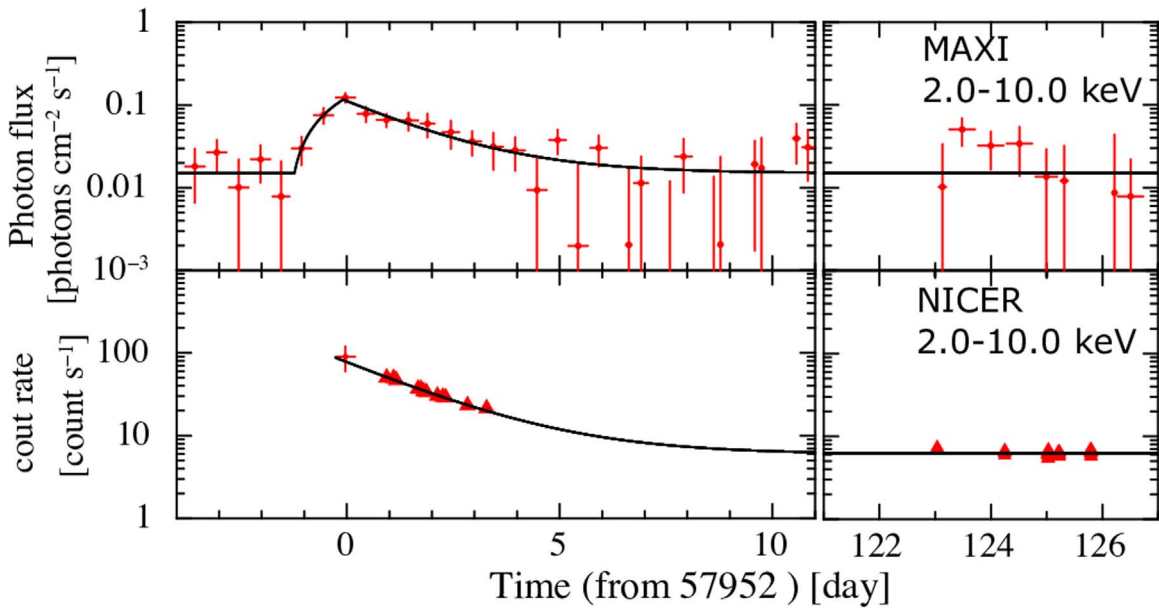


Figure 3. Light curves of FN 11 (see Table 3 for time intervals). The upper panel shows the MAXI photon flux. The lower panel shows the NICER count rate, together with that obtained with MAXI (the first bin). The MAXI data were converted to the NICER count rate with *Web PIMMS*. The horizontal axis is the number of days since MJD = 57,952 (2017 July 18 UT). The solid lines show the fitting function (see text for details).

Table 2
Best-fit Parameters of the MAXI Light Curves and Spectra of GT Mus

Flare ID	kT (keV)	EM (10^{36} cm)	$L_{x,\text{peak}}^a$ (10^{33} erg s $^{-1}$)	χ_{red}^2 (d.o.f.) ^b	τ_r^c (ks)	τ_d (ks)	E_{rise}^d (10^{38} erg)	E_{decay}^d (10^{38} erg)
FN 01	7^{+27}_{-4}	$0.7^{+0.4}_{-0.2}$	$1.0^{+0.2}_{-0.9}$	0.47(6)	...	110^{+80}_{-50}	...	1.2
FN 02	11^{+20}_{-5}	$1.1^{+0.3}_{-0.2}$	$1.9^{+0.4}_{-1.4}$	0.47(7)	90^{+10}_{-20}	140^{+50}_{-40}	0.8	2.6
FN 03	6^{+2}_{-2}	$0.7^{+0.3}_{-0.2}$	$0.8^{+0.2}_{-0.6}$	1.15(6)	70^{+90}_{-20}	110^{+40}_{-30}	0.3	0.9
FN 04	6.6^d	0.7 ± 0.2	0.9 ± 0.2	0.28(6)	120^{+40}_{-60}	100^{+110}_{-50}	0.5	0.9
FN 05	5^{+14}_{-3}	$0.9^{+0.8}_{-0.4}$	$1.0^{+0.3}_{-0.9}$	0.28(3)	...	140^{+180}_{-60}	...	1.3
FN 06	4^{+7}_{-2}	$1.3^{+1.2}_{-0.6}$	$1.0^{+0.2}_{-0.8}$	0.08(3)	60^{+60}_{-30}	140^{+100}_{-60}	0.3	1.4
FN 07	6.6^d	1.5 ± 0.4	2.0 ± 0.4	0.66(6)	120^{+50}_{-40}	360^{+120}_{-80}	1.1	7.3
FN 08	6.6^d	1.0 ± 0.3	1.3 ± 0.3	1.11(5)	90^{+20}_{-30}	240^{+100}_{-80}	0.5	3.2
FN 09	6^{+6}_{-6}	$1.7^{+0.6}_{-0.4}$	$2.0^{+0.4}_{-1.0}$	1.49(10)	80 ± 20	130 ± 40	0.7	2.7
FN 10	9^{+2}_{-3}	$2.3^{+0.5}_{-0.4}$	$3.7^{+0.4}_{-1.0}$	0.59(18)	90 ± 10	95 ± 20	1.6	3.5
FN 11	5^{+11}_{-2}	$1.1^{+0.6}_{-0.4}$	$1.2^{+0.3}_{-0.9}$	0.88(5)	110^{+20}_{-30}	160^{+70}_{-50}	0.6	1.9

Notes. Errors, upper limits, and lower limits refer to 90% confidence intervals.

^a Flare peak luminosity in the 2–20 keV band. The absorption is corrected.

^b Here χ_{red}^2 and d.o.f. stand for reduced χ^2 and degrees of freedom, respectively. Please note that some fittings have very low χ_{red}^2 , primarily due to the low d.o.f., which came from the limited photon statistics.

^c Here τ_r is flare rise time, which is the difference between the flare start time and its peak time.

^d Because the kT was not derived when we made it free, we fixed it to the average value of the other flares.

All of these results indicate that the GT Mus flares are among the hottest, longest, and brightest flares ever observed.

4.2. High Flare Activity

During the MAXI 8 yr observation period, the large flares were detected every year. Although the possibility that GT Mus is always active is not excluded, it is likely that GT Mus was in an active phase over 8 yr.

It is well known that the Sun has an 11 yr sunspot cycle (Schwabe 1844). Its X-class flares ($\sim 10^{31}$ erg) tend to occur in the period near the solar maximum, spanning about a half of a

solar cycle (~ 5.5 yr; Aschwanden & Freeland 2012). On the other hand, activity cycles of other RS CVn-type stars have been obtained from a spot number/area as 14–20 yr for HR 1099 (V711 Tau; Lanza et al. 2006; Muneer et al. 2010; Perdelwitz et al. 2018), 9.2 yr for II Peg (Lindborg et al. 2013), and 15 yr for LQ Hya (Berdyugina et al. 2002). During half of these activity cycles, the stars are active, which is indicative from the existence of many/large spots.

If the same trend in the activity–phase ratio applies to GT Mus, its activity cycle will be at least 16 yr long. Future monitoring observations will determine how long the active phase of GT Mus lasts, if it indeed has a cycle like other active stars.

Table 3
Best-fit Parameters for the NICER Time-resolved Spectra during FN 11

No. ^a	Time Interval ^b days	N_{H}^{c} 10^{20} cm^3	Z^{d} Z_{\odot}	$kT_{\text{hot}}^{\text{e}}$ keV	$\text{EM}_{\text{hot}}^{\text{f}}$ 10^{54} cm^{-3}	$kT_{\text{cool}}^{\text{e}}$ keV	$\text{EM}_{\text{cool}}^{\text{f}}$ 10^{54} cm^{-3}	Count Rate counts s^{-1}	L_{X}^{g} $10^{32} \text{ erg s}^{-1}$	χ_{red}^2 (d.o.f.) ^h
01	T0 + 0.840:T0 + 1.034	5 ± 1	0.3 ± 0.1	$4.5^{+0.4}_{-0.3}$	55 ± 2	$1.05^{+0.26}_{-0.06}$	4^{+8}_{-1}	292 ± 2	9.4 ± 0.1	0.92(240)
02	T0 + 1.097:T0 + 1.098	4 ± 1	0.5 ± 0.1	4.8 ± 0.4	49 ± 2	$1.01^{+0.06}_{-0.08}$	3 ± 1	287 ± 2	$9.3^{+0.1}_{-0.2}$	0.86(219)
03	T0 + 1.162:T0 + 1.163	4 ± 1	0.4 ± 0.1	4.5 ± 0.3	48 ± 2	$1.05^{+0.16}_{-0.05}$	4 ± 1	280 ± 2	8.8 ± 0.1	1.07(248)
04	T0 + 1.676:T0 + 1.678	5 ± 1	0.4 ± 0.1	3.9 ± 0.3	38 ± 2	0.99 ± 0.05	4 ± 1	236 ± 1	7.1 ± 0.1	0.96(250)
05	T0 + 1.741:T0 + 1.743	5 ± 1	0.4 ± 0.1	$4.1^{+0.3}_{-0.2}$	38 ± 1	1.03 ± 0.04	4 ± 1	228 ± 1	6.9 ± 0.1	1.25(239)
06	T0 + 1.805:T0 + 1.807	4 ± 1	0.4 ± 0.1	3.8 ± 0.2	37 ± 1	$1.04^{+0.03}_{-0.04}$	4 ± 1	224 ± 1	$6.57^{+0.04}_{-0.07}$	1.16(294)
07	T0 + 1.870:T0 + 1.872	3 ± 1	0.4 ± 0.1	4.0 ± 0.2	34 ± 1	1.03 ± 0.04	3 ± 1	219 ± 1	6.5 ± 0.1	0.98(260)
08	T0 + 2.128:T0 + 2.130	5 ± 1	0.3 ± 0.1	3.8 ± 0.2	32 ± 2	$0.99^{+0.05}_{-0.06}$	3 ± 1	197 ± 1	5.9 ± 0.1	0.98(249)
09	T0 + 2.256:T0 + 2.259	3^{+2}_{-1}	$0.2^{+0.1}_{-0.2}$	$5.1^{+5.3}_{-0.6}$	$25.5^{+1.9}_{-7.2}$	$1.27^{+0.07}_{-0.10}$	7^{+20}_{-3}	186 ± 1	5.6 ± 0.1	1.03(276)
10	T0 + 2.320:T0 + 2.321	2 ± 1	0.5 ± 0.2	$4.7^{+1.0}_{-0.7}$	25 ± 2	$1.26^{+0.09}_{-0.22}$	4^{+5}_{-2}	185 ± 2	5.4 ± 0.1	1.21(203)
11	T0 + 2.837:T0 + 2.838	6^{+4}_{-1}	$0.2^{+0.1}_{-0.2}$	$3.6^{+2.5}_{-0.4}$	$24.9^{+2.0}_{-8.1}$	$1.03^{+0.33}_{-0.08}$	5^{+8}_{-2}	163 ± 1	4.7 ± 0.1	0.89(201)
12	T0 + 3.284:T0 + 3.285	5^{+2}_{-4}	<0.15	$4 <$	$12.5^{+7.0}_{-1.9}$	$1.29^{+0.07}_{-0.27}$	16^{+9}_{-14}	144 ± 1	$4.4^{+0.1}_{-1.0}$	1.01(161)

Notes. Errors refer to 90% confidence intervals.

^a Serial number of each time interval.

^b The time interval is in units of days. T0 = 57,952 [MJD] (2017 July 18 UT 00:00:00).

^c Hydrogen column density.

^d Metal abundance.

^e Plasma temperature (kT) of the hot and cool components.

^f The EM of the hot and cool components.

^g The X-ray luminosity in the 0.5–10.0 keV band. The absorption is corrected.

^h Here χ_{red}^2 and d.o.f. stand for reduced χ^2 and degrees of freedom, respectively.

4.3. Cooling Process of the GT Mus Flares

We investigate the cooling of the hot component of FN 11, which is the dominant flaring event in the observed flares. Here we apply the quasi-static cooling model of van den Oord & Mewe (1989) as a simple approximation.

In the model, the ratio between the radiative-cooling timescale (τ_r) and the conductive-cooling timescale (τ_c) remains constant during the flare decay phase. The two timescales can be expressed by the following formulae:

$$\tau_r = \frac{3n_e kT}{n_e^2 \Psi(T)}, \quad (1)$$

$$\tau_c = \frac{3n_e kT}{E_c}, \quad (2)$$

where T , n_e , $\Psi(T)$, and E_c are the temperature, electron density, emissivity of an optically thin thermal plasma, and mean conductive energy loss rate, respectively. Here $\Psi(T)$ in Equation (1) is a combination of X-ray emission lines and bremsstrahlung continuum spectrum. In the case of the hot component of FN 11, it is given by $\Psi(T) = \Psi(T_0) T^{-\gamma} = 10^{-24.73} T^{1/4} \text{ erg cm}^3 \text{ s}^{-1}$, since the flare plasma temperature is higher than 20 MK (e.g., Mewe et al. 1985, 1986) throughout the observation.

We assume that the flare geometry is one semicircular loop having a constant cross section, as van den Oord & Mewe (1989) did. Under this assumption, E_c in Equation (2) is expressed by

$$E_c = \frac{16\kappa_0 T^{7/2}}{7L^2}, \quad (3)$$

where κ_0 and L are the plasma thermal conductivity of $8.8 \times 10^{-7} \text{ erg cm}^{-1} \text{ s}^{-1} \text{ K}^{-7/2}$ (Spitzer 1962) and the flare loop

full length, respectively. In this case, from the hydrodynamic equations of conservation of mass, momentum, and energy, the solution yields the scaling law in Kuin & Martens (1982) or Equations (19(b), 19 (c), and (20) in van den Oord & Mewe (1989) and then the ratio τ_r/τ_c of 0.1.

When we assume that the aspect ratio (a : diameter-to-length ratio) and L do not change during a flare, the fact that τ_r/τ_c is not time-variable means that $T^{13/4}/\text{EM}$ is not time-variable either (from Equations (1)–(3); corresponding to Equations (7)–(10) in van den Oord & Mewe 1989). The bottom right panel of Figure 5 shows the value of $T_{\text{hot},7}^{13/4}/\text{EM}_{\text{hot},54}$ as a function of time, where $T_{\text{hot},7}$ and $\text{EM}_{\text{hot},54}$ are $T_{\text{hot}}/(10^7 \text{ K})$ and $\text{EM}_{\text{hot}}/(10^{54} \text{ cm}^{-3})$, respectively. We apply a constant function to this plot and obtain an acceptable fit with $T_{\text{hot},7}^{3.25}/\text{EM}_{\text{hot},54} = 2.9 \pm 0.3$, a χ_{red}^2 value of 0.8, and a d.o.f. of 11. Then, the FN 11 flare can be described with the model.

4.4. Flare Loop Geometry

In the case of quasi-static flare cooling, the decay timescale of kT_{hot} and EM_{hot} can be estimated on the basis of a set of time-evolution formulae expressed in the form of

$$F(t) = F(t') \left(1 + \frac{t-t'}{3\tau_{\text{qs}}} \right)^{-\alpha} \quad (4)$$

according to Equations (26) and (27) in van den Oord & Mewe (1989), where F represents either kT_{hot} or EM_{hot} as a function of time (t). Here τ_{qs} is called the quasi-static timescale, the specific timescale that determines the decay of both kT_{hot} and EM_{hot} . The value of α depends on F : 8/7 and 26/7 for the cases where F is kT_{hot} and EM_{hot} , respectively (van den Oord & Mewe 1989).

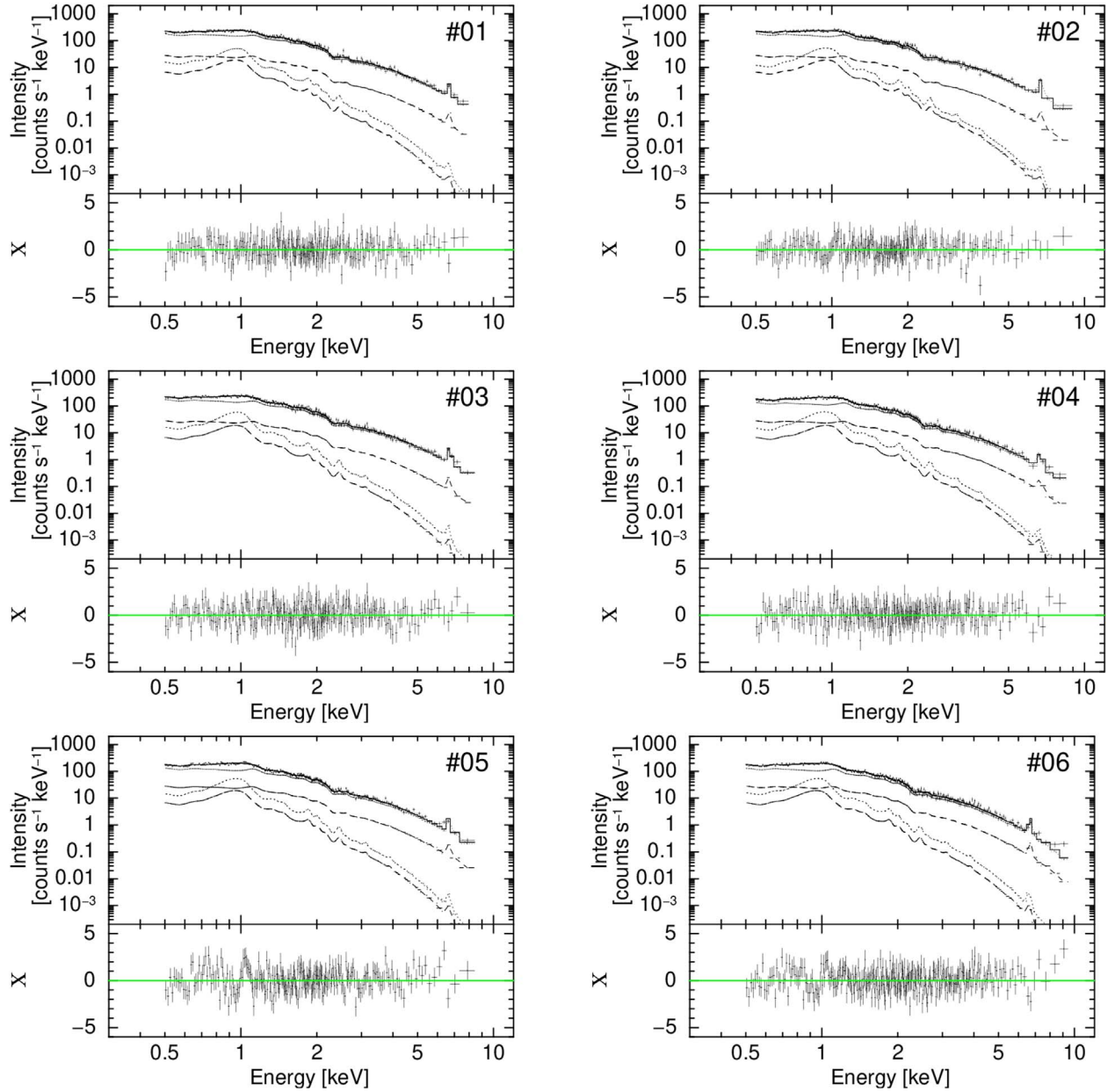


Figure 4. Time-resolved NICER spectra of FN 11 (see Table 3 for time intervals). In each panel, the data and component-separated best-fit model (total model, flare hot-/cool-temperature components, and quiescent hot-/cool-temperature components, shown by solid, dotted, and dashed lines, respectively) are shown in the upper panel, whereas the χ values are shown in the lower panel.

We fit the time variation of kT_{hot} and EM_{hot} obtained with MAXI and NICER with Equation (4) simultaneously, with the common parameter τ_{qs} free. The parameter t' is set to -0.032 (MJD = 57,951.968), which corresponds to the epoch at which the peak of kT_{hot} and EM_{hot} were observed with MAXI. Then we obtained $\tau_{\text{qs}} = 130 \pm 4$ ks, $kT_{\text{hot}}(t') = 5.7 \pm 0.2$ keV, and $\text{EM}_{\text{hot}}(t') = 99 \pm 2$ with $\chi^2_{\text{red}}/\text{d.o.f.} = 0.89/22$. The best-fit models are shown in the time variation of kT_{hot} and EM_{hot} in the center two figures on the right panel of Figure 5, while the model for $L_{\text{X,hot}}$ is calculated from those for kT_{hot} and EM_{hot} and inserted in the upper right panel.

We estimate from these values the three geometric parameters of FN 11 of flare loop length L , aspect ratio of the loop a , and electron density n_e using the following equations of the quasi-static cooling model (van den Oord & Mewe 1989;

Tsuboi et al. 2000),

$$a = 1.38 \left(\frac{\tau_{\text{qs}}}{10 \text{ ks}} \right)^{-1/2} \left\{ \frac{kT_{\text{hot}}(t')}{\text{keV}} \right\}^{-33/16} \left\{ \frac{\text{EM}_{\text{hot}}(t')}{10^{54} \text{ cm}^{-3}} \right\}^{1/2}, \quad (5)$$

$$L = 1.0 R_{\odot} \frac{\tau_{\text{qs}}}{10 \text{ ks}} \left\{ \frac{kT_{\text{hot}}(t')}{\text{keV}} \right\}^{7/8}, \quad (6)$$

$$n_e = 4.4 \times 10^{10} \text{ cm}^{-3} \left(\frac{\tau_{\text{qs}}}{10 \text{ ks}} \right)^{-1} \left\{ \frac{kT_{\text{hot}}(t')}{\text{keV}} \right\}^{3/4}, \quad (7)$$

and obtain the following:

$$a = 0.11 \pm 0.02, \quad (8)$$

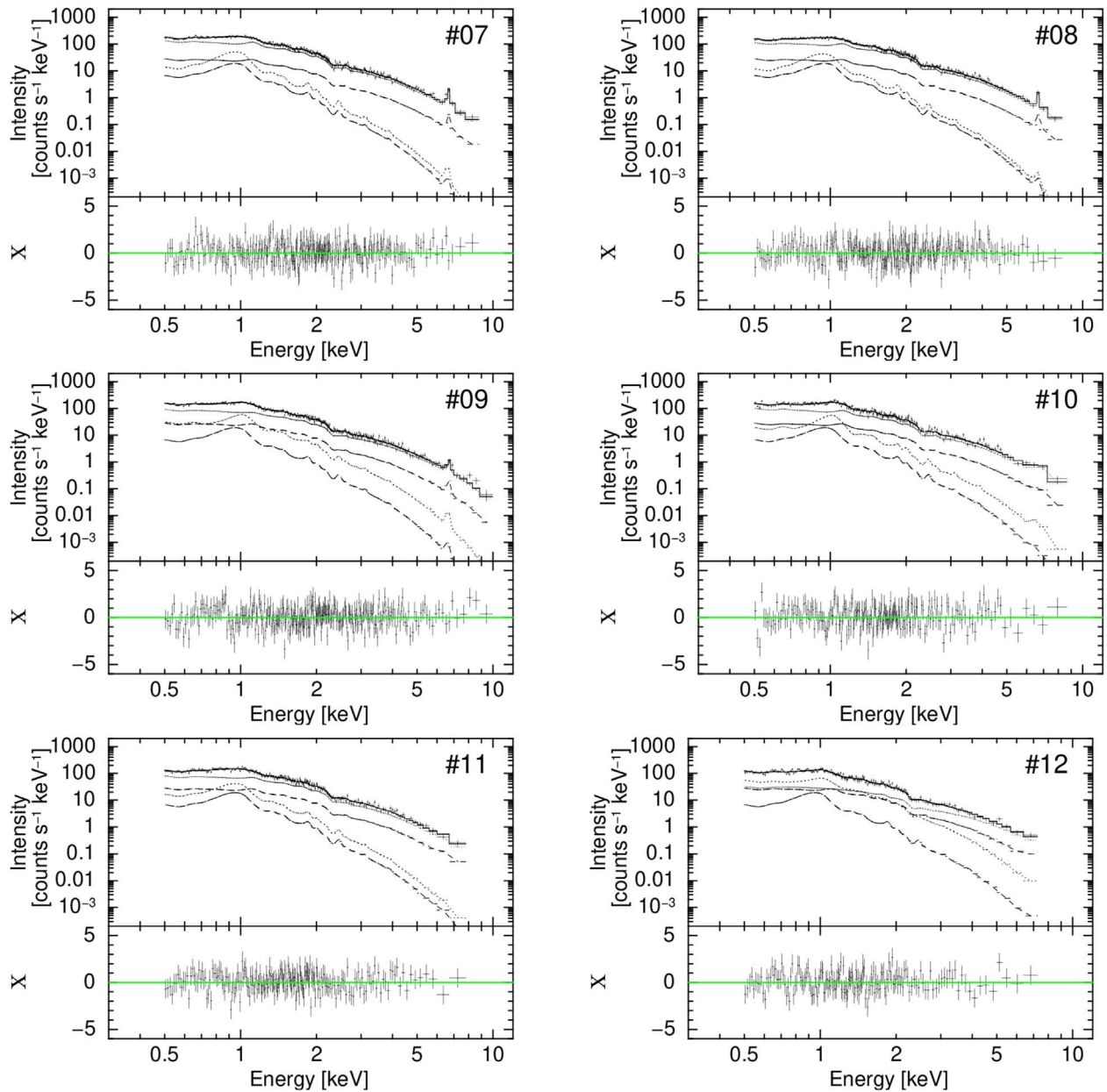


Figure 4. (Continued.)

$$L = (4.2 \pm 0.2) \times 10^{12} \text{ [cm]} \quad (61 \pm 5R_{\odot}), \quad (9)$$

$$n_e = (1.3 \pm 0.1) \times 10^{10} \text{ [cm}^{-3}\text{]}. \quad (10)$$

The estimated loop length L is much larger, by two orders of magnitude, than that of the typical solar flare, 10^9 – 10^{10} cm (Kontar et al. 2011). Pandey & Singh (2012a) made comprehensive loop length comparisons of RS CVn-type stars using pointed observations (e.g., XMM-Newton). They found loop lengths of 10^{10} – 10^{12} cm. On the other hand, MAXI has observed large flares from RS CVn-type stars that have a loop length of 10^{11} – 10^{13} cm (Tsuboi et al. 2016). The derived loop length in this work is among the highest in the MAXI flare sample. The derived GT Mus loop length is then almost four times larger than the stellar radius, $16.56 R_{\odot}$ (1.2×10^{12} cm; Gaia Collaboration et al. 2016, 2018). There are the MAXI/GSC sources that have flares with loop lengths of up to an order of magnitude larger than the stellar radius; our derived

ratio of L relative to the stellar radius of GT Mus ranges within the nominal range for these other MAXI stellar flares. Note that the binary separation of HD 101379 is unknown; hence, we are unable to tell whether the loop is connected between the RS CVn-type stars.

The estimated parameter, a , is within the range for solar active-region loops (0.06–0.2; Golub et al. 1980). The footprints of the loop cover $\sim 3.7\%$ of the stellar surface (6.7×10^{23} cm²). The estimated density n_e is consistent with the typical solar and stellar flares of 10^{10} – 10^{13} cm⁻³ (Aschwanden & Benz 1997; Güdel 2004; Reale 2007).

4.5. Coronal Magnetic Activity

In this section, we examine the magnetic activity of GT Mus. As for low-mass ($< 1.5 M_{\odot}$) main-sequence stars, one of the indicators of magnetic activity, the X-ray to bolometric luminosity ratio (L_X/L_{bol}), is well known to show a good

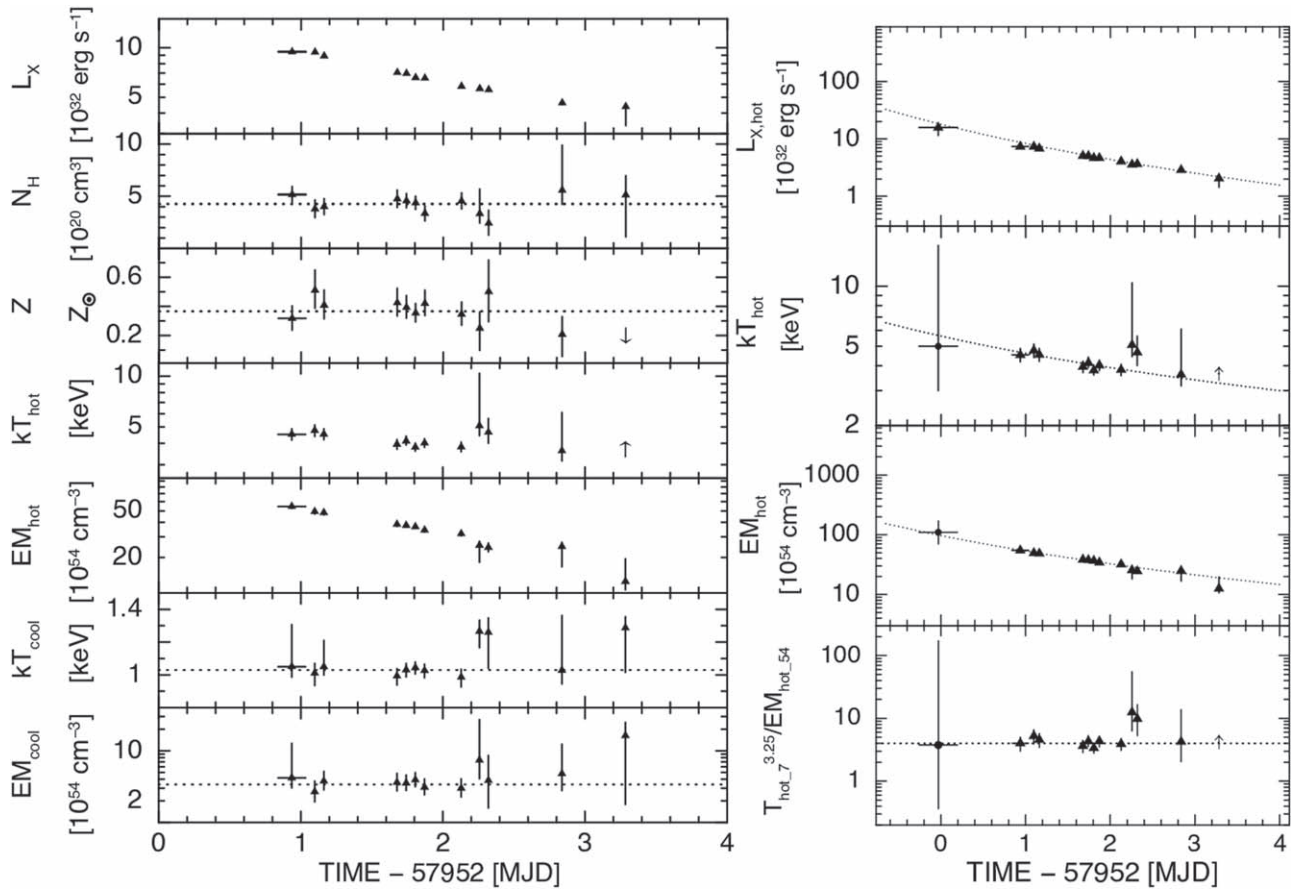


Figure 5. (Left) From top to bottom, the time variations of the luminosity in the 0.5–10 keV band in units of 10^{32} erg s^{-1} , hydrogen column density in 10^{20} cm^3 , metal abundance compared to solar abundance, temperatures of the hot and cool plasma components in keV, and their EMs in 10^{54} cm^{-3} are shown for FN 11 from the NICER time-resolved spectra (Table 3). Dotted lines are the best-fit models summarized in Table 4. (Right) Time variation of the parameters obtained for the hot component. The first bin is from MAXI data, while the other bins are from NICER data. From the top, the luminosity in the 0.5–10 keV band, the temperature, the EM, and the ratio of $T_{hot}^{3.25}/EM_{hot}$ are shown. Dotted lines in the panels for T_{hot} and EM_{hot} show the best-fit model for Equation (4). The dotted line in the luminosity plot is calculated from the models for T_{hot} and EM_{hot} . In all panels, the NICER and MAXI data are shown by triangles and circles, respectively.

Table 4

Best-fit Parameters of the Stable Parameters in Table 3 with a Constant Model

	N_H (10^{20} cm^3)	Z (Z_\odot)	kT_{cool} (keV)	EM_{cool} (10^{54} cm^{-3})
C ^a	4.2 ± 0.3	0.37 ± 0.03	$1.03^{+0.01}_{-0.02}$	3.4 ± 0.4
χ^2_{red} ^b	0.7	0.6	0.8	0.3

Notes. Errors refer to 90% confidence intervals. The d.o.f. of all the fitting is 11.

^a Fitting result of time series with a constant function.

^b Reduced χ^2 .

correlation to the Rossby number (R_o), which is the ratio of the rotation period to the convective turnover timescale (e.g., Wright et al. 2011). Whereas the data show a distinctive log-linear relation between L_X/L_{bol} and R_o for $R_o \gtrsim 0.1$, the relationship is flat for $R_o \lesssim 0.1$. This flattening indicates saturation of magnetic activity. In contrast, as for the intermediate-mass giant binaries like GT Mus, which has a mass of $M_* = 2.7 M_\odot$ (Tokovinin 2008), the relation has not yet been established, though some studies exist for a period–activity relationship using the other parameters (e.g., Gondoin 2007).

We replotted the data points of 20 G- and K-type intermediate-mass giant binaries in Gondoin (2007), changing

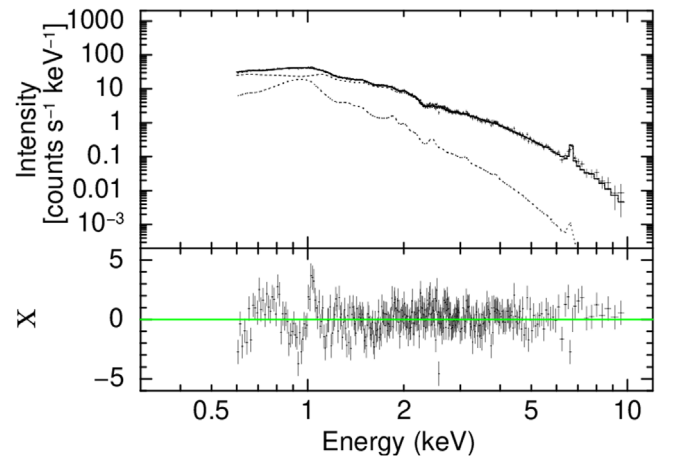


Figure 6. Time-averaged quiescent-state spectra. The data and component-separated best-fit model (the total model and its hot-/cool-temperature components are shown with solid and dashed lines, respectively) are shown in the upper panel, whereas the χ values are shown in the lower panel.

the vertical axis of the surface X-ray flux to L_X/L_{bol} and keeping the independent variable as R_o (see their Figure 2, right panel). Here R_o and L_{bol} are used from Gondoin (2007), calculated with the stellar parameters taken from the literature (Schrijver & Zwaan 1991; Strassmeier et al. 1993; Hummel et al. 1994;

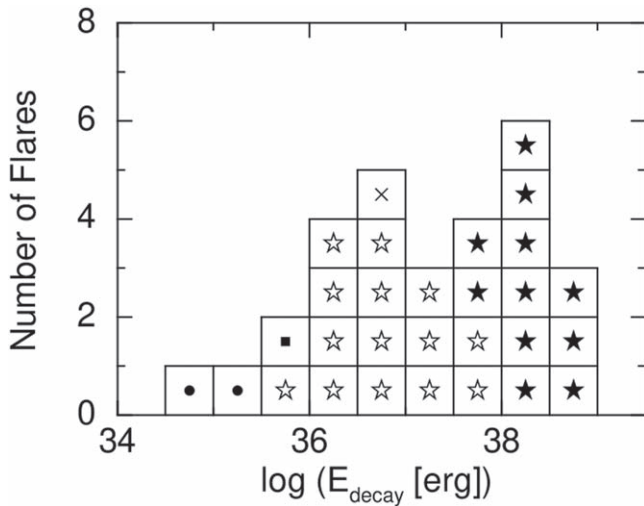


Figure 7. Flare energies of GT Mus compared with those from other stars reported in Tsuboi et al. (2016). Filled stars, open stars, filled circles, filled squares, and crosses in boxes indicate GT Mus, RS CVn-type stars (except for GT Mus), dMe stars, Algol, and TWA 7, respectively. The flare energies of the other flares, extracted from Tsuboi et al. (2016), were recalculated using the distances of the Gaia DR2 catalog (Gaia Collaboration et al. 2016, 2018).

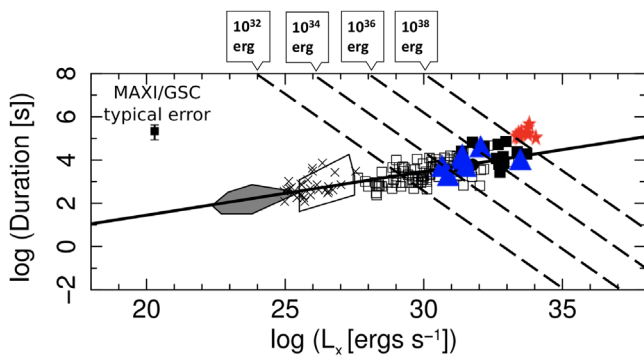


Figure 8. Universal correlation of the duration of flares vs. bolometric X-ray luminosity obtained by Tsuboi et al. (2016), which is established from solar flares to large stellar flares. The blue triangles are RS CVn-type flares (Nordon & Behar 2007; Pandey & Singh 2012a; Drake et al. 2014; Gong et al. 2016; Osten et al. 2007). The red stars are GT Mus flares from this work. The dashed lines show total released flare energies of 10^{32} – 10^{38} erg.

McDowell et al. 1994; Voges et al. 1999; Kovári et al. 2001; Williamon et al. 2005). Each L_X is taken from the ROSAT bright source catalog (Voges et al. 1999) in order to unify the X-ray band with that used in Wright et al. (2011), 0.1–2.4 keV. The distribution of data points for the giant binaries is found to agree with the relation derived from that of late-type main-sequence stars (see Figure 9).

We then evaluated GT Mus in the diagram. The value R_o of GT Mus is derived to be 0.614 from the rotation period of 61.4 days (Murdoch et al. 1995) and the convective turnover timescale of 100 days, the latter of which was obtained from a function of effective temperature during the evolution of a $2.2 M_\odot$ star (Gunn et al. 1998). Here the effective temperature (4761 K) is taken from the Gaia Collaboration et al. (2016, 2018). The L_{bol} was calculated to be 4.9×10^{35} erg from the effective temperature and stellar radius of $16.56 R_\odot$. With extrapolation of the quiescent-state spectrum of NICER, the value of L_X is estimated to be $7.18 \pm 0.02 \times 10^{32}$ erg s^{-1} in

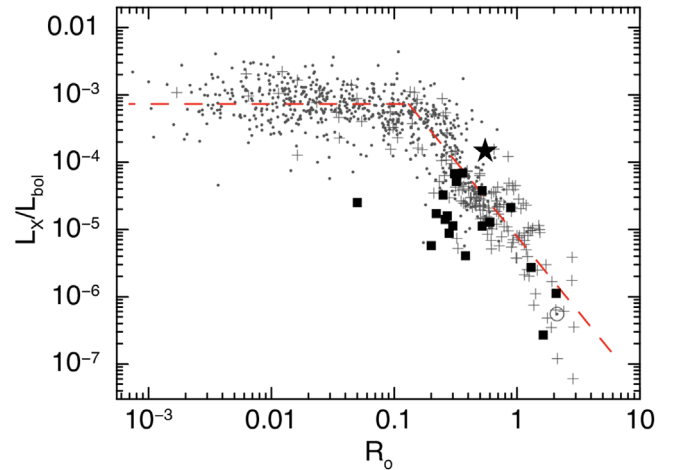


Figure 9. Scatter plot of the X-ray to bolometric luminosity ratio (L_X/L_{bol}) vs. Rossby number (R_o). Dots and plus signs are for late-type main-sequence single and binary stars, respectively. The solar symbol is for the Sun (Wright et al. 2011). Squares are for G- and K-type giant binaries (Gondoin 2007). The star indicates GT Mus.

the 0.1–2.4 keV band. Figure 9 compares the location of GT Mus with other stars in the L_X/L_{bol} – R_o diagram.

We find that GT Mus is consistent with the trend followed by late-type main-sequence stars and G- and K-type giant binaries. However, we note that GT Mus shows a considerably higher L_X/L_{bol} ratio than the other giant binaries in the diagram. This high X-ray fraction supports the idea that GT Mus is in an active phase.

5. Summary

1. MAXI detected 11 flares from the RS CVn-type star GT Mus in its 8 yr of all-sky X-ray monitoring observations. The released energies during the decay phases of the flares were in the range of 1 – 11×10^{38} erg in the 0.1–100 keV band, which is higher than any other stellar flares detected in 2 yr of monitoring observations with MAXI (Tsuboi et al. 2016), as well as the other flares detected with the other missions. The released energies during the whole duration ($\tau_r + \tau_d$) were in the range of 2 – 13×10^{38} erg in the same band. The flare parameters (kT , EM, X-ray luminosity in the 0.1–100 keV band, and τ_d) are found to be located at the upper end of the known parameter correlation plot of stellar flares compiled by Tsuboi et al. (2016), suggesting that these flares have the largest energy ever observed from stellar flares.
2. We performed a 3 day follow-up X-ray observation of GT Mus with NICER from 2017 July 18, 1.5 days after the MAXI detection of a large flare. The time-resolved spectra suggest that the flare cooled quasi-statically during the NICER observation. On the basis of a quasi-static cooling model, the flare loop size is estimated to be $4.2 \pm 0.2 \times 10^{12}$ cm ($61 \pm 5 R_\odot$). This size is 2–3 orders of magnitude larger than that of the typical solar flare loop of 10^9 – 10^{10} cm.
3. For the first time, we plotted the G and K giant binary samples in the diagram of X-ray to bolometric luminosity ratio versus Rossby number and obtained a consistent distribution with those for the low-mass stars. The Rossby number and $\log(L_X/L_{\text{bol}})$ of GT Mus are 0.614 and -3.5 , respectively, which puts GT Mus in line with

the relation derived from low-mass and giant binary stars in the diagram. It shows a considerably higher L_X/L_{bol} than other giant binaries. This high X-ray fraction suggests that GT Mus is at a high magnetic activity level, which is consistent with what is inferred from its recurring large flares.

This research used MAXI data provided by RIKEN, JAXA, and the MAXI team. This work was supported by NASA through the NICER team and the Astrophysics Explorers Program. It used data and software provided by the High Energy Astrophysics Science Archive Research Center (HEASARC), a service of the Astrophysics Science Division at NASA/GSFC and the High Energy Astrophysics Division of the Smithsonian Astrophysical Observatory. The authors thank Kazunari Shibata for useful discussions and comments on the cooling process. R.S. acknowledges financial support from the Junior Research Associate Program in RIKEN, JSPS Overseas Challenge Program for Young Researchers and Research Assistant Program in Chuo University. Y.T. acknowledges financial support from JSPS KAKENHI grant No. JP17K05392. W.I. acknowledges support from the Special Postdoctoral Researchers Program in RIKEN and JSPS KAKENHI grant No. JP16K17717. Y.M. gratefully acknowledges funding from the Tanaka Kikinzoku Memorial Foundation. M.S. acknowledges financial support from JSPS KAKENHI grant No. JP16K17672.

ORCID iDs

Ryo Sasaki  <https://orcid.org/0000-0003-3756-6684>
 Yohko Tsuboi  <https://orcid.org/0000-0001-9943-0024>
 Wataru Iwakiri  <https://orcid.org/0000-0002-0207-9010>
 Satoshi Nakahira  <https://orcid.org/0000-0001-9307-046X>
 Yoshitomo Maeda  <https://orcid.org/0000-0002-9099-5755>
 Keith Gendreau  <https://orcid.org/0000-0001-7115-2819>
 Michael F. Corcoran  <https://orcid.org/0000-0002-7762-3172>
 Kenji Hamaguchi  <https://orcid.org/0000-0001-7515-2779>
 Craig B. Markwardt  <https://orcid.org/0000-0001-9803-3879>
 Teruaki Enoto  <https://orcid.org/0000-0003-1244-3100>
 Tatehiro Mihara  <https://orcid.org/0000-0002-6337-7943>
 Megumi Shidatsu  <https://orcid.org/0000-0001-8195-6546>
 Hitoshi Negoro  <https://orcid.org/0000-0003-0939-1178>

References

- Aschwanden, M. J., & Benz, A. O. 1997, *ApJ*, **480**, 825
 Aschwanden, M. J., & Freeland, S. L. 2012, *ApJ*, **754**, 112
 Berdyugina, S. V., Pelt, J., & Tuominen, I. 2002, *A&A*, **394**, 505
 Collier, A. C. 1982, PhD thesis, Univ. Canterbury
 Drake, J. J., Ratzlaff, P., Kashyap, V., et al. 2014, *ApJ*, **783**, 2
 Freund, S., Robrade, J., Schneider, P. C., & Schmitt, J. H. M. M. 2018, *A&A*, **614**, A125
 Gaia Collaboration, Brown, A. G. A., Vallenari, A., et al. 2018, *A&A*, **616**, A1
 Gaia Collaboration, Prusti, T., de Bruijne, J. H. J., et al. 2016, *A&A*, **595**, A1
 Gendreau, K. C., Arzoumanian, Z., Adkins, P. W., et al. 2016, *Proc. SPIE*, **9905**, 99051H
 Golub, L., Maxson, C., Rosner, R., Vaiana, G. S., & Serio, S. 1980, *ApJ*, **238**, 343
 Gondoin, P. 2007, *A&A*, **464**, 1101
 Gong, H., Osten, R., Maccarone, T., et al. 2016, *RAA*, **16**, 131
 Güdel, M. 2004, *A&ARv*, **12**, 71
 Gunn, A. G., Mitrou, C. K., & Doyle, J. G. 1998, *MNRAS*, **296**, 150
 Houk, N., & Cowley, A. P. 1975, Univ. Michigan Catalogue of Two-dimensional Spectral Types for the HD Stars (Ann Arbor, MI: Dept. of Astronomy, Univ. Michigan)
 Hummel, C. A., Armstrong, J. T., Quirrenbach, A., et al. 1994, *AJ*, **107**, 1859
 Kanetou, S., Negoro, H., Tsuboi, Y., et al. 2015, *ATel*, **8285**, 1
 Kontar, E. P., Hannah, I. G., & Bian, N. H. 2011, *ApJL*, **730**, L22
 Kovári, Z., Strassmeier, K. G., Bartus, J., et al. 2001, *A&A*, **373**, 199
 Kuin, N. P. M., & Martens, P. C. H. 1982, *A&A*, **108**, L1
 Lanza, A. F., Piluso, N., Rodonò, M., Messina, S., & Cutispoto, G. 2006, *A&A*, **455**, 595
 Lindborg, M., Mantere, M. J., Olsper, N., et al. 2013, *A&A*, **559**, A97
 Matsuoka, M., Kawasaki, K., Ueno, S., et al. 2009, *PASJ*, **61**, 999
 McAlister, H., Hartkopf, W. I., & Franz, O. G. 1990, *AJ*, **99**, 965
 McDowell, E. J., Plummer, D., Prestwich, A., et al. 1994, The Einstein Observatory Soft X-ray Source List (CD-ROM), IPC Data Archive
 Mewe, R., Gronenschild, E. H. B. M., & van den Oord, G. H. J. 1985, *A&AS*, **62**, 197
 Mewe, R., Lemen, J. R., & van den Oord, G. H. J. 1986, *A&AS*, **65**, 511
 Mihara, T., Nakajima, M., Sugizaki, M., et al. 2011, *PASJ*, **63**, S623
 Muneer, S., Jayakumar, K., Rosario, M. J., Raveendran, A. V., & Mekkaden, M. V. 2010, *A&A*, **521**, A36
 Murdoch, K. A., Hearnshaw, J. B., Kilmartin, P. M., & Gilmore, A. C. 1995, *MNRAS*, **276**, 836
 Nakahira, S., Ebisawa, K., & Negoro, H. 2013, JAXA Research and Development Report JAXA-RR-12-006, Japan Aerospace Exploration Agency (JAXA), 29
 Nakajima, M., Suwa, F., Negoro, H., et al. 2010, *ATel*, **3021**, 1
 Negoro, H., Kohama, M., Serino, M., et al. 2016, *PASJ*, **68**, S1
 Nordon, R., & Behar, E. 2007, *A&A*, **464**, 309
 Osten, R. A., Drake, S., Tueller, J., et al. 2007, *ApJ*, **654**, 1052
 Pandey, J. C., & Singh, K. P. 2012a, *MNRAS*, **419**, 1219
 Perdelwitz, V., Navarrete, F. H., Zamponi, J., et al. 2018, *A&A*, **616**, A161
 Prigozhin, G., Gendreau, K., Foster, R., et al. 2012, *Proc. SPIE*, **8453**, 845318
 Reale, F. 2007, *A&A*, **471**, 271
 Sasaki, R., Nakamura, Y., Tsuboi, Y., et al. 2016, *ATel*, **9251**, 1
 Scargle, J. D., Norris, J. P., Jackson, B., & Chiang, J. 2013, *ApJ*, **764**, 167
 Schrijver, C. J., & Zwaan, C. 1991, *A&A*, **251**, 183
 Schwabe, H. 1844, *AN*, **21**, 233
 Shibata, K., & Yokoyama, T. 1999, *ApJL*, **526**, L49
 Smith, R. K., Brickhouse, N. S., Liedahl, D. A., & Raymond, J. C. 2001, *ApJL*, **556**, L91
 Spitzer, L. 1962, *Physics of Fully Ionized Gases* (New York: Interscience)
 Strassmeier, K. G., Hall, D. S., Fekel, F. C., & Scheck, M. 1993, *A&AS*, **100**, 173
 Strassmeier, K. G., Hall, D. S., Zeilik, M., et al. 1988, *A&AS*, **72**, 291
 Tokovinin, A. 2008, *MNRAS*, **389**, 925
 Tsuboi, Y., Imanishi, K., Koyama, K., Grosso, N., & Montmerle, T. 2000, *ApJ*, **532**, 1089
 Tsuboi, Y., Koyama, K., Murakami, H., et al. 1998, *ApJ*, **503**, 894
 Tsuboi, Y., Yamazaki, K., Sugawara, Y., et al. 2016, *PASJ*, **68**, 90
 Uzawa, A., Tsuboi, Y., Morii, M., et al. 2011, *PASJ*, **63**, S713
 van den Oord, G. H. J., & Mewe, R. 1989, *A&A*, **213**, 245
 Voges, W., Aschenbach, B., Boller, T., et al. 1999, *A&A*, **349**, 389
 Williamson, R. M., Van Hamme, W., Torres, G., Sowell, J. R., & Ponce, V. C. 2005, *AJ*, **129**, 2798
 Wilms, J., Allen, A., & McCray, R. 2000, *ApJ*, **542**, 914
 Wright, N. J., Drake, J. J., Mamajek, E. E., & Henry, G. W. 2011, *ApJ*, **743**, 48